



# Stabilization of catalyst particles against sintering on oxide supports with high oxygen ion lability exemplified by Ir-catalyzed decomposition of N<sub>2</sub>O



Ioannis V. Yentekakis <sup>a,\*</sup>, Grammatiki Goula <sup>a</sup>, Paraskevi Panagiotopoulou <sup>a</sup>, Stavroula Kampouri <sup>a</sup>, Martin J. Taylor <sup>b,c</sup>, Georgios Kyriakou <sup>b,c,\*</sup>, Richard M. Lambert <sup>d,e,\*</sup>

<sup>a</sup> Laboratory of Physical Chemistry & Chemical Processes, School of Environmental Engineering, Technical University of Crete, GR-73100 Chania, Crete, Greece

<sup>b</sup> European Bioenergy Research Institute, Aston University, Aston Triangle, Birmingham B4 7ET, United Kingdom

<sup>c</sup> Chemical Engineering and Applied Chemistry, Aston University, Aston Triangle, Birmingham B4 7ET, United Kingdom

<sup>d</sup> Chemistry Department, Cambridge University, Cambridge CB2 1EW, United Kingdom

<sup>e</sup> Instituto de Ciencia de Materiales de Sevilla (CSIC), Americo Vespucio 49, 41092 Seville, Spain

## ARTICLE INFO

### Article history:

Received 11 January 2016

Received in revised form 15 March 2016

Accepted 6 April 2016

Available online 7 April 2016

### Keywords:

Sintering  
Nanoparticle stabilization  
Oxide supports  
Oxygen ion lability  
Ostwald ripening  
Particle diffusion  
Catalytic N<sub>2</sub>O decomposition  
Iridium  
Iridium oxide  
Ceria  
Gadolinia  
Zirconia  
Alumina

## ABSTRACT

Iridium nanoparticles deposited on a variety of surfaces exhibited thermal sintering characteristics that were very strongly correlated with the lability of lattice oxygen in the supporting oxide materials. Specifically, the higher the lability of oxygen ions in the support, the greater the resistance of the nanoparticles to sintering in an oxidative environment. Thus with  $\gamma$ -Al<sub>2</sub>O<sub>3</sub> as the support, rapid and extensive sintering occurred. In striking contrast, when supported on gadolinia-ceria and alumina-ceria-zirconia composite, the Ir nanoparticles underwent negligible sintering. In keeping with this trend, the behavior found with yttria-stabilized zirconia was an intermediate between the two extremes. This resistance, or lack of resistance, to sintering is considered in terms of oxygen spillover from support to nanoparticles and discussed with respect to the alternative mechanisms of Ostwald ripening versus nanoparticle diffusion. Activity towards the decomposition of N<sub>2</sub>O, a reaction that displays pronounced sensitivity to catalyst particle size (large particles more active than small particles), was used to confirm that catalytic behavior was consistent with the independently measured sintering characteristics. It was found that the nanoparticle active phase was Ir oxide, which is metallic, possibly present as a capping layer. Moreover, observed turnover frequencies indicated that catalyst-support interactions were important in the cases of the sinter-resistant systems, an effect that may itself be linked to the phenomena that gave rise to materials with a strong resistance to nanoparticle sintering.

© 2016 The Authors. Published by Elsevier B.V. This is an open access article under the CC BY license (<http://creativecommons.org/licenses/by/4.0/>).

## 1. Introduction

The deactivation of catalyst nanoparticles as a result of thermal sintering is an important problem that has received much attention both for reasons of fundamental significance [1–3] and because it is a leading cause of the degradation of industrial catalysts used for large-scale synthesis of commodity chemicals of global importance [4–6] and of catalytic systems that play a critical role in environmental protection [7–9].

Two mechanisms have been invoked and extensively discussed in regard to the sintering of supported nanoparticles—Ostwald

ripening (OR) versus particle diffusion and coalescence (PD). Distinguishing between the two on the basis of *ex situ* TEM analyses of samples subjected to a variety of sintering protocols is non-trivial, and often not possible. For an up to date conspectus see Ref. [10] and references therein. However, recent investigations in which *in situ* TEM methods were used to study both model systems (Pt/Al<sub>2</sub>O<sub>3</sub>) [11] and practical dispersed catalysts (Ni/MgAl<sub>2</sub>O<sub>4</sub>) [12] provided direct evidence that OR was by far the dominant mechanism in both cases, which are themselves chemically distinctly different. In some cases resistance to sintering is mediated by very specific interactions such as epitaxy [13,14] or by so-called metal-support interactions [15–17].

Here we report on the sintering and de-N<sub>2</sub>O catalytic behavior of well-characterized Ir nanoparticles supported on four different oxides with very different oxygen ion labilities at elevated temperatures, ranging from  $\gamma$ -Al<sub>2</sub>O<sub>3</sub>, through yttria-

\* Corresponding authors.

E-mail addresses: [yentek@isc.tuc.gr](mailto:yentek@isc.tuc.gr) (I.V. Yentekakis), [G.Kyriakou@aston.ac.uk](mailto:G.Kyriakou@aston.ac.uk) (G. Kyriakou), [rml1@cam.ac.uk](mailto:rml1@cam.ac.uk) (R.M. Lambert).

stabilized zirconia (YSZ:  $Zr_{0.92}Y_{0.08}O_{2-\delta}$ ) to gadolinia doped ceria (GDC:  $Ce_{0.9}Gd_{0.1}O_{2-\delta}$ ) and alumina-ceria-zirconia (ACZ: 80 wt% $Al_2O_3$ +10 wt% $CeO_2$ -10 wt% $ZrO_2$ ). We introduce the qualitative term “oxygen lability” because oxygen ion mobilities are not available for all four oxides. By combining available mobility values with our experimentally determined oxygen storage capacity (OSC) data a correlation between these properties may be established which enables us to rank these oxides as indicated above, in terms of their propensity to provide spillover oxygen [18–25]. The object was to examine whether the sintering behavior of a particular catalyst (Ir) supported on a range of materials with very different oxygen labilities would give insight into effects, and therefore principles, that could be more broadly applicable. In fact, a very strong correlation was found between the lability of lattice oxygen in the supports and the resistance to sintering at high temperature of iridium nanoparticles supported on them. Thus Ir/ $\gamma$ - $Al_2O_3$  exhibited rapid and extensive sintering, whereas Ir/GDC and Ir/ACZ were essentially impervious to sintering, with Ir/YSZ exhibiting intermediate behavior. We consider alternative possible explanations in terms of either OR or PD for the remarkable very strong resistance to sintering of Ir/GDC and Ir/ACZ.

Catalytic  $N_2O$  decomposition, an environmentally important [26–30] and well-studied reaction [31–35] with known particle size dependence [36] was used to verify that under conditions of steady-state catalytic reaction the behavior of the four systems was indeed consistent with their independently measured sintering characteristics. Catalysis of this reaction by Ir is of interest in its own right because it is relatively little studied compared to catalysis by Pt, Pd and Rh, even though Ir shows superior performance to that of Pt and Pd [36–42]. The particle size dependence of Ir-catalyzed  $N_2O$  decomposition has now been clearly established, and also the oxidation state of Ir under reaction conditions. Moreover, in the case of supports characterized by high oxygen lability, which strongly favored the persistence of small catalyst particles, catalyst-support interaction altered turnover frequencies—an effect that may be linked to the phenomena that also gave rise to materials with a strong resistance to nanoparticle sintering.

## 2. Experimental

### 2.1. Materials

The fresh catalysts consisted of iridium nanoparticles supported on  $\gamma$ - $Al_2O_3$ , YSZ, GDC, and ACZ with low Ir metal loading (0.4–0.7 wt%, Table 1). Powders of  $\gamma$ - $Al_2O_3$  (Engelhard), 8 mol% yttria stabilized zirconia (Zirconia sales, UK Ltd.) and 10 mol% gadolinia doped ceria (Anan Kasei Co, Ltd.) were impregnated under continuous stirring at 75 °C in a solution of  $IrCl_3 \cdot H_2O$  (Abcr GmbH & Co.KG) of appropriate concentration. The ACZ support was made in house by co-precipitation [25] of the metal nitrate precursors,  $Al(NO_3)_3 \cdot 9H_2O$ ,  $Zr(NO_3)_2 \cdot H_2O$ ,  $Ce(NO_3)_3 \cdot 6H_2O$  (Alfa Aesar, 99.5%) followed by calcination, and impregnated as above. These precursor materials were dried at 110 °C for 12 h, heated at 400 °C for 2 h under 50%  $H_2/He$  flow ( $50 \text{ cm}^3 \text{ min}^{-1}$ ) followed by heating at 850 °C for 1 h under 1%  $H_2/He$  flow ( $50 \text{ cm}^3 \text{ min}^{-1}$ ) to yield the corresponding catalysts, hereafter referred to as “fresh”. As we shall see the reduction step after drying of the catalysts is responsible for the formation of small metallic Ir particles on the surface of the oxide supports. Contrary to this, when an oxidation step takes place before the  $H_2$ -reduction of the catalyst suspension large Ir particles can form [36,42].

In order to establish the relative susceptibilities of the four types of catalyst toward sintering, all were subject to the same aging protocol as follows: two consecutive cycles of 1 h oxidation (20%  $O_2/He$ ,  $50 \text{ cm}^3 \text{ min}^{-1}$ , 750 °C) followed by 0.5 h reduction (2%

$H_2/He$ ,  $50 \text{ cm}^3 \text{ min}^{-1}$ , 750 °C), hereafter referred to as “aged”, after which the effects of aging were examined by a variety of methods as described below.

### 2.2. Materials characterization methods

Textural, structural and morphological characteristics of the fresh and aged samples were determined by a variety of techniques involving  $N_2$  adsorption-desorption (BET), hydrogen chemisorption, hydrogen temperature programmed reduction ( $H_2$ -TPR), inductively coupled plasma optical emission spectroscopy (ICP-OES), high resolution transmission electron microscopy (HRTEM) and powder X-ray diffraction (PXRD).

BET surface areas were obtained from  $N_2$  adsorption-desorption isotherms done at  $-196^\circ\text{C}$  using a Nova 2200e, Quantachrome instrument at relative pressures in the range of 0.05–0.30. Total pore volumes were calculated from the  $N_2$  volume sorbed at the highest relative pressure. Prior to these measurements the samples were degassed at  $350^\circ\text{C}$  for 12 h under vacuum.

Hydrogen chemisorption measurements provided corroborating information regarding the number of Ir surface sites and associated crystallite sizes. Data were acquired with a Quantachrome/ChemBet Pulsar TPR/TPD chemisorption analyzer with simultaneous use of a thermal conductivity detector and an Omnistar/Pfeiffer Vacuum mass spectrometer. For this purpose, 100–300 mg catalyst samples were pretreated as follows before  $H_2$ -chemisorption measurements. All samples were reduced with a 1% $H_2/He$  mixture ( $15 \text{ cm}^3 \text{ min}^{-1}$ ) at  $400^\circ\text{C}$  for 1 h, followed by  $N_2$  ( $15 \text{ cm}^3 \text{ min}^{-1}$ ) at  $400^\circ\text{C}$  for 0.5 h, then cooled to room temperature under  $N_2$  flow. To avoid hydrogen spillover phenomena in the case of  $CeO_2$ -containing supports, samples were cooled to  $0^\circ\text{C}$  in an ice/water bath. Pulses of pure hydrogen ( $280 \mu\text{L}$ ) were injected until saturation and the total hydrogen uptake (chemisorbed  $H_2$ ) was determined from which value the hydrogen to metal (H/Ir) ratio and the mean Ir crystallite size were calculated.

$H_2$ -TPR measurements were carried out to determine the oxygen storage capacity (OSC) of the four supports using a quartz U tube loaded with  $\sim 150$  mg of support, using the same TPR/TPD apparatus as that employed for  $H_2$  chemisorption measurements. Before data acquisition, samples were oxidized in situ with 20%  $O_2/He$  at  $750^\circ\text{C}$  for 30 min followed by cooling to room temperature in flowing oxygen. The system was then purged under He flow for 10 min and the TPR measurements carried out with a flow of  $15 \text{ cm}^3/\text{min}$  of 1%  $H_2/He$  at  $10^\circ\text{C min}^{-1}$  to  $900^\circ\text{C}$ . Subsequently, the temperature was maintained at  $900^\circ\text{C}$  until hydrogen consumption profiles returned to their initial values.

Aberration-corrected High resolution TEM measurements were carried out at Birmingham University (JEOL 2100F operated at 200 kV).

Iridium contents were determined by inductively coupled plasma optical emission spectroscopy (Thermo Scientific iCAP 7400 duo) after microwave digestion of the samples in 5 mL  $HNO_3$  (Fisher, 70%) and 100 mg  $NH_4F$  (Sigma Aldrich,  $\geq 98.0\%$ ) at  $190^\circ\text{C}$  (CEM–MARS microwave reactor) followed by dilution in 10% aqueous  $HNO_3$ . Powder X-ray diffraction was performed on a Bruker D8 Advance diffractometer using monochromated  $Cu K\alpha_1$  radiation ( $\lambda = 0.1542 \text{ nm}$ ).

### 2.3. Catalytic activity measurements

Catalytic testing and stability measurements were carried out in a continuous flow apparatus equipped with a single pass reactor operated in both differential (low conversion) and light-off (high conversion) modes. It consisted of a feed unit and an analysis unit utilizing on-line gas chromatography (Shimadzu GC-2014, thermal

**Table 1**

Textural properties of fresh and aged catalysts.

Catalyst <sup>a</sup>	Catalyst condition	$S_{\text{BET}}$ ( $\text{m}^2 \text{ g}^{-1}$ )	Total pore volume ( $\text{cm}^3 \text{ g}^{-1}$ )	Average pore size diameter (nm)
0.7 wt% Ir/ $\gamma$ -Al <sub>2</sub> O <sub>3</sub>	Fresh	158.7	0.550	13.87
	Aged	140.1	0.310	8.90
0.7 wt% Ir/YSZ	Fresh	4.1	0.008	8.18
	Aged	4.5	0.009	7.75
0.4 wt% Ir/GDC	Fresh	10.0	0.036	14.16
	Aged	10.4	0.016	6.08
0.4 wt% Ir/ACZ	Fresh	72.6	0.216	11.89
	Aged	63.6	0.203	12.74

<sup>a</sup> Iridium content determined by inductively coupled plasma optical emission spectroscopy (ICP-OES).

conductivity detector, He carrier gas) equipped with molecular sieve 5A and HayeSep D columns. The feed composition was 1000 ppm N<sub>2</sub>O balanced with He. The tubular, quartz, fixed-bed, single-pass reactor (internal diameter 3 mm) was loaded with 50 mg catalyst (grain size 180–250  $\mu\text{m}$ ) held between two quartz wool plugs for catalytic activity measurements. For turnover frequency measurements, the total feed flow rate ( $F_t$ ) was varied between 20 and 200  $\text{cm}^3 \text{ min}^{-1}$  in order to maintain N<sub>2</sub>O conversion at less than  $\sim 15\%$ , thus ensuring that the reactor was operated under differential conditions. N<sub>2</sub>O conversion performance was evaluated by light-off measurements carried out in the temperature range 300–550 °C at a constant total gas flow rate of 150  $\text{cm}^3 \text{ min}^{-1}$  corresponding to a weight-based hourly space velocity of 180,000  $\text{cm}^3 \text{ g}^{-1} \text{ h}^{-1}$ . Catalyst bed temperature measurement was by means of a centrally located K-type thermocouple.

### 3. Results and discussion

#### 3.1. Characterization

##### 3.1.1. Textural analysis

The textural characteristics of the fresh and aged catalysts are summarized in Table 1. Only marginal changes in the total surface areas were observed, even after high temperature aging.

Table 2 summarizes H<sub>2</sub> chemisorption data for both fresh and aged catalysts. All the fresh catalysts exhibited small Ir particles ( $\sim 1\text{--}2 \text{ nm}$ ), regardless of the nature and surface area of the support, despite the large variation in the latter quantity. However, the aged samples showed a very strong dependence of Ir catalyst particle size on the support. Thus in the most susceptible catalyst, Ir/ $\gamma$ -Al<sub>2</sub>O<sub>3</sub>, underwent extensive growth of the Ir particles from 0.8 to 28.8 nm. The effect of aging was significantly less with the YSZ support (2.2  $\rightarrow$  22.6 nm), and almost negligible with the CeO<sub>2</sub>-containing supports (1.5  $\rightarrow$  1.8 nm for GDC and 1.8  $\rightarrow$  1.6 nm for ACZ). These pre- and post aging particle size estimates are in broad agreement with those obtained from HRTEM (see Table 2). The apparent discrepancy between the H<sub>2</sub> chemisorption and HRTEM data in the cases of aged Ir/ $\gamma$ -Al<sub>2</sub>O<sub>3</sub> and Ir/YSZ is due the presence of individual particles together with large aggregates of particles (Fig. 3). However, the key conclusion is that Ir/ $\gamma$ -Al<sub>2</sub>O<sub>3</sub> underwent a very high degree of sintering in striking contrast to Ir/GDC and Ir/ACZ, both of which were extremely resistant to sintering.

The OSC of the four supports was assessed via H<sub>2</sub>-TPR as described above (Fig. 1), yielding values of 0, 5.7, 116 and 185.45  $\mu\text{mol O}_2/\text{g}$  for  $\gamma$ -Al<sub>2</sub>O<sub>3</sub>, YSZ, ACZ and GDC respectively. As expected, in accord with the literature,  $\gamma$ -Al<sub>2</sub>O<sub>3</sub> and YSZ showed negligible and very small OSC respectively, whereas ACZ and GDC exhibited substantial capacity. The higher capacity of GDC is to be expected as it contains a higher proportion of CeO<sub>2</sub> than does ACZ ( $\sim 90\%$  versus  $\sim 10\%$ ). Note however that the redox behavior (i.e. oxygen lability) of ACZ was activated at a significantly lower temperature ( $\sim 300^\circ\text{C}$ ) than for GDC ( $\sim 500^\circ\text{C}$ ). As we shall see, this

has important implications for N<sub>2</sub>O decomposition catalyzed by Ir particles supported on ACZ and GDC.

##### 3.1.2. Structural and morphological analysis (PXRD, TEM)

Representative PXRD data for fresh and aged Ir/ $\gamma$ -Al<sub>2</sub>O<sub>3</sub>, Ir/YSZ, Ir/GDC and Ir/ACZ catalysts are shown in Fig. 2a–d respectively. The diffractogram for fresh Ir/ $\gamma$ -Al<sub>2</sub>O<sub>3</sub> (Fig. 2a) shows reflections characteristic of  $\gamma$ -Al<sub>2</sub>O<sub>3</sub> at  $2\theta = 37.7^\circ$ ,  $46^\circ$  and  $67^\circ$ . Diffraction peaks corresponding to Ir were undetectable, as expected, due to the small size of these nanoparticles, as indeed demonstrated by H<sub>2</sub> chemisorption and HRTEM (Table 2). In contrast, the aged Ir/ $\gamma$ -Al<sub>2</sub>O<sub>3</sub> catalyst showed clear reflections at  $2\theta = 40.7^\circ$ ,  $47.3^\circ$  and  $69.1^\circ$  due to large crystalline Ir particles (28.4 nm, Scherrer) in good quantitative agreement with the value obtained by H<sub>2</sub> chemisorption (Table 2). None were detected in the cases of aged Ir/GDC and aged Ir/ACZ, again in good agreement with H<sub>2</sub> chemisorption and HRTEM.

In order to determine which of the steps (oxidation or reduction) in our aging procedure had the most effect on catalyst particle sintering, additional tests were carried out with Ir/ $\gamma$ -Al<sub>2</sub>O<sub>3</sub> the most vulnerable system of all. Fig. 3 shows the changes in Ir particle size when the sample was subjected to either (i) a sequence of reduction steps (aging procedure P1) or (ii) a number of different oxidation or oxidation + reduction steps (aging procedures P2–P5); details given in caption of Fig. 3. These results clearly demonstrate that reduction had a minimal effect on Ir particle size: metallic Ir is resistant to sintering. However, when an oxidation step was involved in the aging process, the Ir particle size increased substantially.

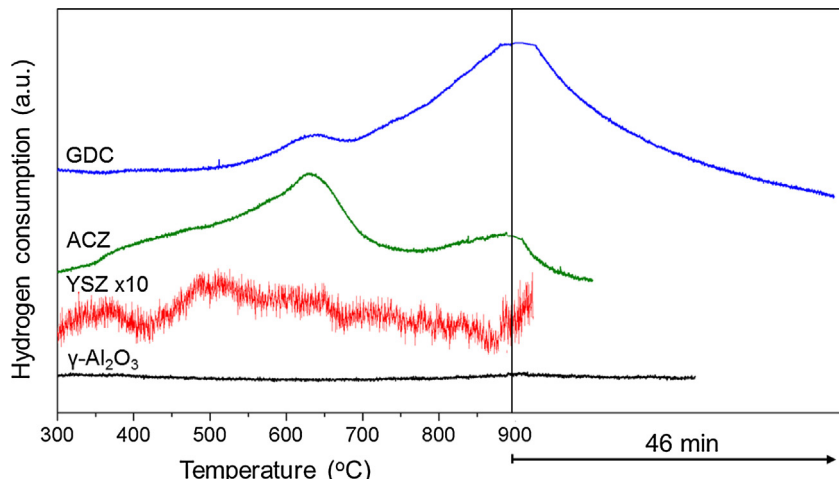
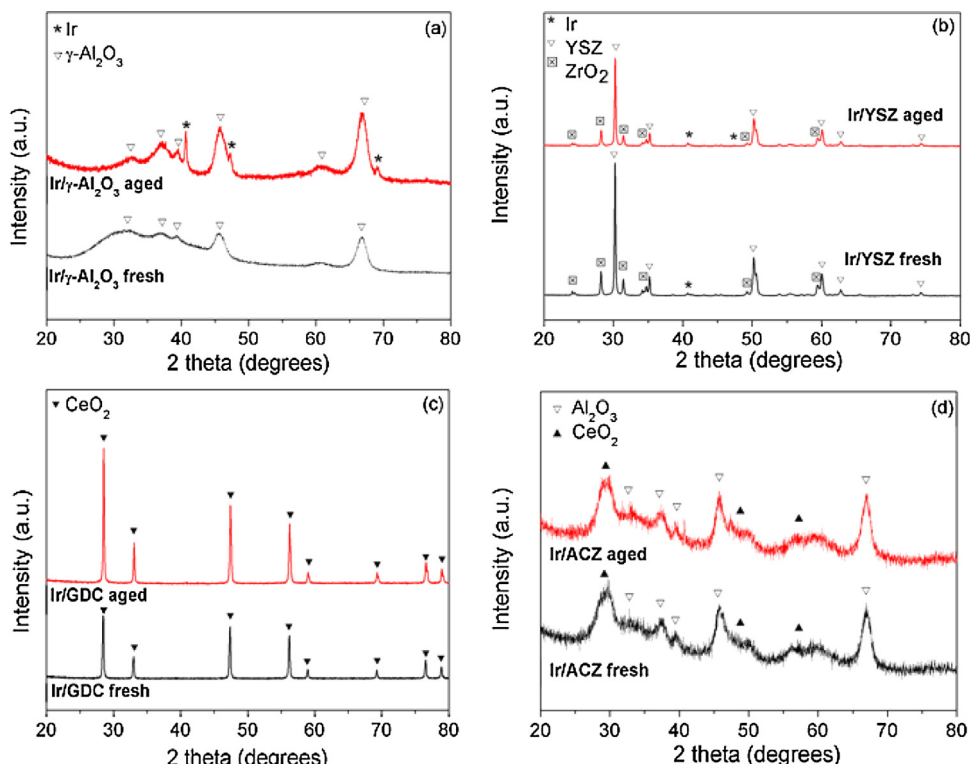
Fig. 4 shows representative HRTEM images of the four catalysts before and after aging (Ir particle sizes are summarized in Table 2). The corresponding particle size distribution data for the fresh and aged samples are shown in Fig. 5. The fresh samples exhibited small, randomly distributed spherical particles. However, the Ir particle morphology of some aged catalysts was substantially different from that of the corresponding fresh materials. Aged Ir/ $\gamma$ -Al<sub>2</sub>O<sub>3</sub> (Fig. 3a) exhibited large aggregates of smaller sintered crystallites, with sizes up to 150 nm, in addition to smaller isolated particles. Similarly, in aged Ir/YSZ, most of the Ir particles (Fig. 4b) showed significant changes in shape and substantial increases in size (10.5 nm) compared to the fresh sample. In contrast, the nanoparticles on the aged Ir/GDC and aged Ir/ACZ retained their original small size and uniform spatial distribution (Fig. 4c).

Even though the present results of themselves do not permit a distinction to be made between the alternative models of either Ostwald ripening or particle diffusion, it is nevertheless useful to consider the observed sintering behavior in terms of both possibilities. A definitive answer awaits investigation by *in situ* TEM methodology as implemented for example by Simonsen et al. [11] and DeLaRiva et al. [12] which technique is beyond our capability.

In regard to OR, it may be that the effective activation energy for atomic or molecular surface diffusion [43] is much higher on the supports that exhibit high oxygen ion lability due to the presence of surface oxygen vacancies that act as traps for diffusing species. With

**Table 2**Active surface area characteristics of the catalysts: H<sub>2</sub> uptake; Ir crystallite sizes; dispersions (H/Ir); particles shapes.

Catalyst	H <sub>2</sub> uptake (cm <sup>3</sup> /g <sub>cat</sub> )		Mean Ir crystallite size (nm)		(H/Ir) <sup>a</sup>		Crystallite shape <sup>d</sup>	
	Fresh	Aged	Fresh H <sub>2</sub> -chem <sup>a</sup> /XRD <sup>b</sup> /TEM <sup>c</sup>	Aged H <sub>2</sub> -chem <sup>a</sup> /XRD <sup>b</sup> /TEM <sup>c</sup>	Fresh	Aged	Fresh	Aged
Ir/γ-Al <sub>2</sub> O <sub>3</sub>	0.392	0.011	0.8/na/1.2	28.8/28.4/14.5 (150) <sup>e</sup>	0.880	0.025	Sp.	Irreg/Sp
Ir/YSZ	0.145	0.014	2.2/na/1.2	22.6/28.7/10.5 (34) <sup>f</sup>	0.326	0.032	Sp.	Sp/Irrg
Ir/GDC	0.121	0.103	1.5/na/1.7	1.8/na/2.0	0.476	0.405	Sp.	Sp.
Ir/ACZ	0.103	0.114	1.8/na/1.8	1.6/na/1.9	0.405	0.448	Sp.	Sp.

<sup>a</sup> Estimated from H<sub>2</sub>-chemisorption data.<sup>b</sup> Estimated from XRD data (Scherrer approximation); na: not applicable due to very small particle size.<sup>c</sup> Particles size values estimated by HRTEM data.<sup>d</sup> Shape from HRTEM images. Sp.: spherical particle shape; Irreg.: Irregular large bifurcate agglomerates of smaller entities.<sup>e</sup> Agglomerated particles up to 150 nm, isolated particles mean diameter 14.5 nm.<sup>f</sup> Agglomerated particles up to 34 nm, isolated particles mean diameter 10.5 nm.**Fig. 1.** H<sub>2</sub>-TPR profiles obtained from the γ-Al<sub>2</sub>O<sub>3</sub>, YSZ, GDC and ACZ supports. Experimental conditions: w<sub>support</sub> = 150 mg; F<sub>t</sub> = 15 cm<sup>3</sup> min<sup>-1</sup> (1%H<sub>2</sub>/He); β = 10 °C min<sup>-1</sup>. For pretreatment conditions see text for discussion.**Fig. 2.** PXRD diffractograms of fresh and aged (a) Ir/γ-Al<sub>2</sub>O<sub>3</sub>, (b) Ir/YSZ, (c) Ir/GDC and (d) Ir/ACZ samples. Aging procedure described in text.

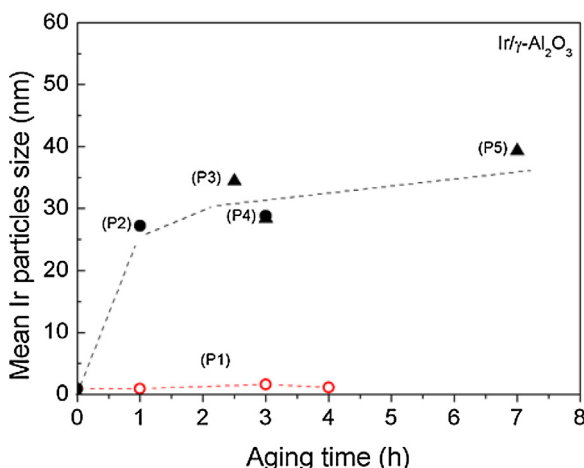


**Fig. 3.** Effect of aging procedures (P1–P5) on Ir particle size of the Ir/γ-Al<sub>2</sub>O<sub>3</sub> catalyst, as estimated by H<sub>2</sub>-chemisorption (cycles) or from XRD data (triangles). Aging procedures: P1: 1, 3, or 4 h reduction at 750 °C; P2: 1 h oxidation at 750 °C; P3: 2 h oxidation followed by 0.5 h reduction at 800 °C; P4: two cycles of 1 h oxidation followed by 0.5 h reduction at 750 °C; P5: 2 h oxidation followed by 0.5 h reduction at 600 °C, then 2 h oxidation followed by 0.5 h reduction at 700 °C and finally 2 h oxidation at 800 °C. Reduction gas: 2% H<sub>2</sub>/He, flow: 50 cm<sup>3</sup> min<sup>-1</sup>. Oxidation gas: 20% O<sub>2</sub>/He, flow: 50 cm<sup>3</sup> min<sup>-1</sup>.

respect to PD, the formation of an electrical double layer due to lattice oxygen spillover from the support to the catalyst nanoparticle, as described by Vernoux et al. [19] could endow the particle with a net negative charge (on its outer gas-exposed surface through the effective double layer [O<sup>δ-</sup> – δ<sup>+</sup>](M) [44,45]) leading to inter-particle repulsion at short range, thus preventing particle–particle encounters followed by coalescence. Such spillover effects would be strongest in the case of supports with high oxygen ion lability, and could operate with nanoparticles consisting of Ir, IrO<sub>2</sub>, or composites of the two (IrO<sub>2</sub> is an electronic conductor) as demonstrated by Nicole et al. [46] and by Peng-Ont et al. [47]. Distinguishing between these alternative explanations would be at least as difficult as the task of differentiating between OR and PD has proved to be, and would require further work that is beyond the scope of the present paper. Under oxidizing conditions, oxygen vacancies in the ceria-based supports are likely to have been saturated or almost saturated with oxygen. This labile lattice oxygen could bond with small Ir particles forming IrO<sub>ce</sub> or CeIrO<sub>ce</sub> bonds, as proposed by Hirata et al. [17] and Nagai et al. [48], resulting in stabilization against sintering of metal nanoparticles supported on oxygen-saturated ceria. In our case, under the OR mechanism, such an effect would immobilize Ir particles and inhibit their agglomeration. Alternatively, under the PD model, the presence of surplus mobile oxygen in the support would enhance formation of the O<sup>δ-</sup> double layer on the surface of the Ir nanoparticles thus impeding their agglomeration by diffusion and coalescence. Whatever the case, it is very clear that supports with high oxygen ion lability endow catalyst nanoparticles with great sintering resistance under oxidizing conditions in comparison those that do not exhibit high oxygen ion lability. Which is the principal message of this paper.

In order to confirm that the strong implications of the ex situ aging experiments correspond to actual catalytic behavior in the case of a relatively simple reaction, we examined the activity of all four catalysts towards the decomposition of pure N<sub>2</sub>O. This process, which occurs in an oxidizing environment, was chosen because it has been well studied and exhibits a marked and well-known particle size dependence [36]. In fact, contrary to normal expectation, in this case small particles are less active than large ones. It should be kept in mind that our object was *not* to make an optimized de-N<sub>2</sub>O catalyst. Rather, it was to use the known characteristics of this

reaction to confirm that the key conclusion drawn from oxidative aging data also held true under conditions of steady state catalytic reaction.

### 3.2. N<sub>2</sub>O decomposition

#### 3.2.1. Activity versus time on stream and the state of the catalyst

The time-on-stream stability of both fresh and aged catalysts was tested at a constant temperature at 450 °C. In all cases, N<sub>2</sub>O conversion increased progressively with time on stream, then stabilized after ~5–7 h (Ir/γ-Al<sub>2</sub>O<sub>3</sub> and Ir/YSZ) or ~10–12 h (Ir/GDC and Ir/ACZ). This is consistent with slow oxidation of Ir particles under the mildly oxidizing conditions, leading to formation of surface IrO<sub>2</sub>, likely the catalytically active phase [36].

To elucidate this point, the experiments summarized in Fig. 6 were carried out. Aged Ir/γ-Al<sub>2</sub>O<sub>3</sub> was first reduced (5% H<sub>2</sub>/He, F<sub>t</sub> = 150 cm<sup>3</sup> min<sup>-1</sup>, 450 °C, 30 min), then run under N<sub>2</sub>O decomposition until steady state, followed by being subjected to a strongly oxidizing atmosphere (20% O<sub>2</sub>/He flow, F<sub>t</sub> = 150 cm<sup>3</sup> min<sup>-1</sup>, 450 °C, 30 min) then repeating N<sub>2</sub>O decomposition, then more vigorous oxidation, (500 °C, 30 min) and finally N<sub>2</sub>O decomposition again. These results are consistent with increasing catalytic activity as initially metallic Ir particles became progressively oxidized under N<sub>2</sub>O decomposition, eventually achieving a steady state activity that remained unaffected by two subsequent stages of strong oxidation with O<sub>2</sub>. Thus the catalytically active phase is likely to have been Ir oxide, as proposed by Ohnishi et al. [36], or a superficial overlayer of IrO<sub>2</sub>. A similar conclusion was reached in the case of N<sub>2</sub>O decomposition catalyzed by Rh [39], which like Ir, is relatively readily oxidized. A definitive answer could be provided by operando XRD, which is beyond our capability.

#### 3.2.2. Turnover frequency

Kinetic measurements were carried out under differential conditions (<15%, N<sub>2</sub>O conversion) after sufficient time on-stream in order to ensure stable operation. Fig. 7a shows turnover frequencies (TOFs) at 400 °C for the fresh and aged catalysts and Fig. 7b shows corresponding Arrhenius plots; activation energies calculated from these, for all fresh and aged samples, are given in Table 3.

The differences between the low and high oxygen ion lability supports is striking (Fig. 7a). Aged Ir/γ-Al<sub>2</sub>O<sub>3</sub> and Ir/YSZ exhibit, respectively, much higher and substantially higher TOFs than their fresh counterparts. This is consistent with their sintering behavior and the known particle size dependence of Ir catalysts in N<sub>2</sub>O decomposition; large particles are more active than small particles [36]. On the other hand, the behavior of Ir/GDC and Ir/ACZ was exactly the opposite, aging actually *decreased* the TOFs, even though both these catalysts underwent a small but detectable degree of sintering, which might otherwise have been expected to result in correspondingly small *increases* in TOF. The diminished activity of Ir/GDC and Ir/ACZ as a result of aging is in line with the activation energies (Fig. 7a and Table 3). This suggests that oxidative aging of these two catalysts on the high oxygen ion lability supports may reduce their already intrinsically low activity as a result of catalyst–support interaction, an effect that has been invoked to account for catalyst stabilization on ceria-based supports [15–17,48] and which should be strongest for very small particles in intimate contact with the support, as is the case here. The nature of such catalyst–support interactions cannot be deduced from our results, but it may well be associated with enhanced spillover of lattice oxygen, an effect that is invoked above as a possible cause for the resistance to sintering of the Ir/GDC and Ir/ACZ catalysts.

#### 3.2.3. Light-off behavior

The dramatic effect of crystallite size on the intrinsic kinetics (TOF) of the Ir catalysts is also apparent in their light-off behavior

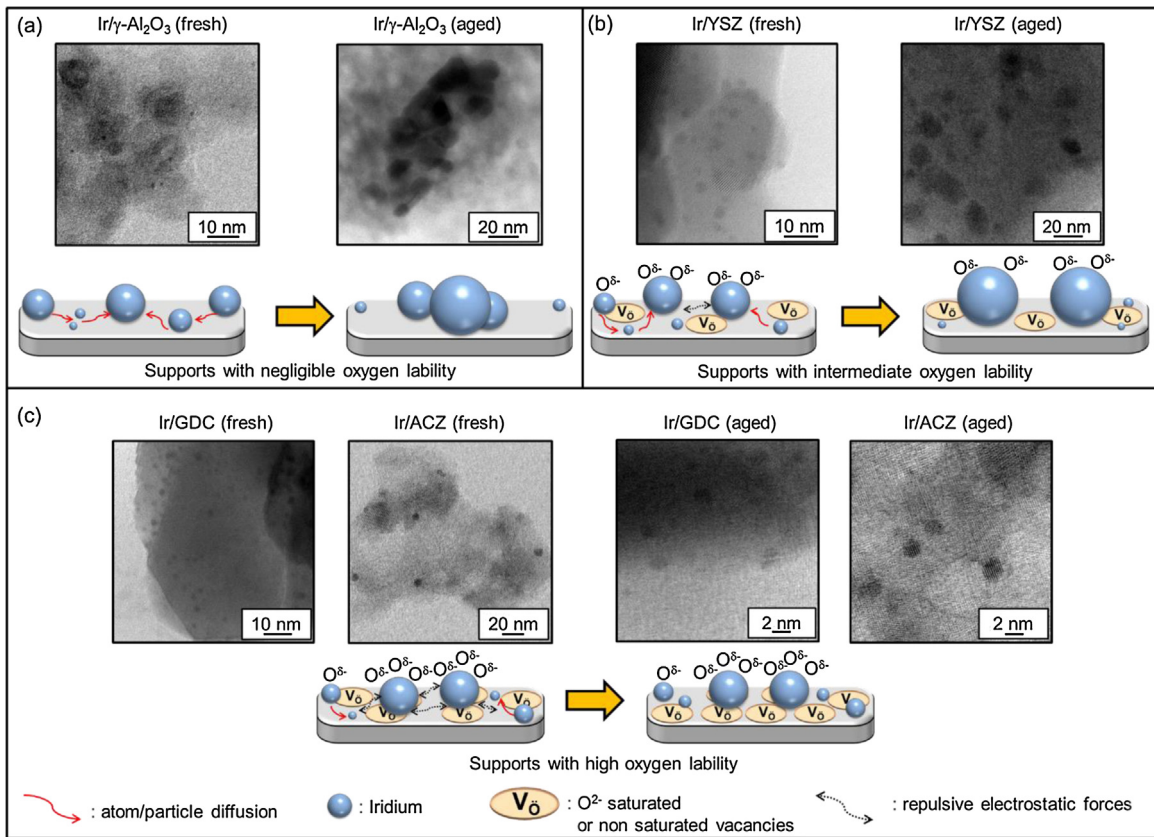


**Fig. 4.** TEM images of fresh and aged samples; (a) Ir/γ-Al<sub>2</sub>O<sub>3</sub>, (b) Ir/YSZ and (c) Ir/GDC and Ir/ACZ. Also shown are possible models for catalyst particle nanoparticle stabilization on supports with high oxygen ion lability and storage capacity.

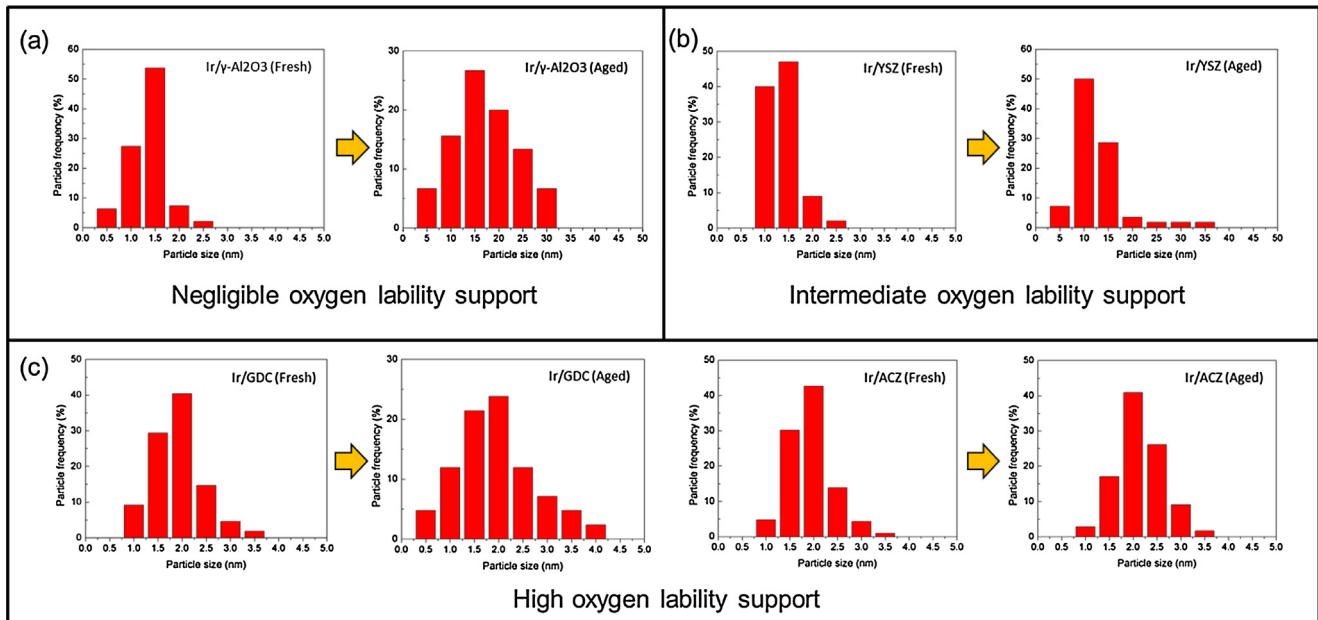


**Fig. 5.** TEM size distribution profiles for fresh and aged samples; (a) Ir/γ-Al<sub>2</sub>O<sub>3</sub>, (b) Ir/YSZ and (c) Ir/GDC and Ir/ACZ.

(Fig. 8). The light-off performance of the fresh samples, which all contained highly dispersed Ir (~1–2 nm), followed the order Ir/γ-Al<sub>2</sub>O<sub>3</sub> > Ir/YSZ > Ir/GDC > Ir/ACZ. This is in good agreement with TOF results shown in Fig. 7, and suggests that the O<sup>δ-</sup> layer created on catalyst particles interfaced with intermediate or high oxygen ion lability supports acts to inhibit deN<sub>2</sub>O activity. According to

Vayenas and coworkers [19,44] this effective O<sup>δ-</sup> layer is expected to weaken the chemisorption bond of electron acceptor adsorbates such as N<sub>2</sub>O<sub>ads</sub> and O<sub>ads</sub> (arising from N<sub>2</sub>O dissociation). To a first approximation, weakening the chemisorption bonds of both N<sub>2</sub>O<sub>ads</sub> and O<sub>ads</sub> should have opposite effects on the reaction rate in terms

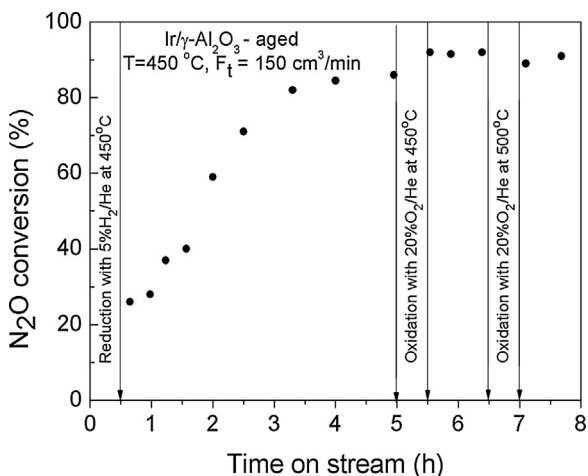


**Fig. 6.** State of the Ir phase for the aged  $\text{Ir}/\gamma\text{-Al}_2\text{O}_3$  catalyst as a function of time on stream.  $T = 450^\circ\text{C}$ , 1000 ppm  $\text{N}_2\text{O}/\text{He}$ , total flow  $F_t = 150 \text{ cm}^3 \text{ min}^{-1}$ ,  $w_{\text{cat}} = 50 \text{ mg}$ .

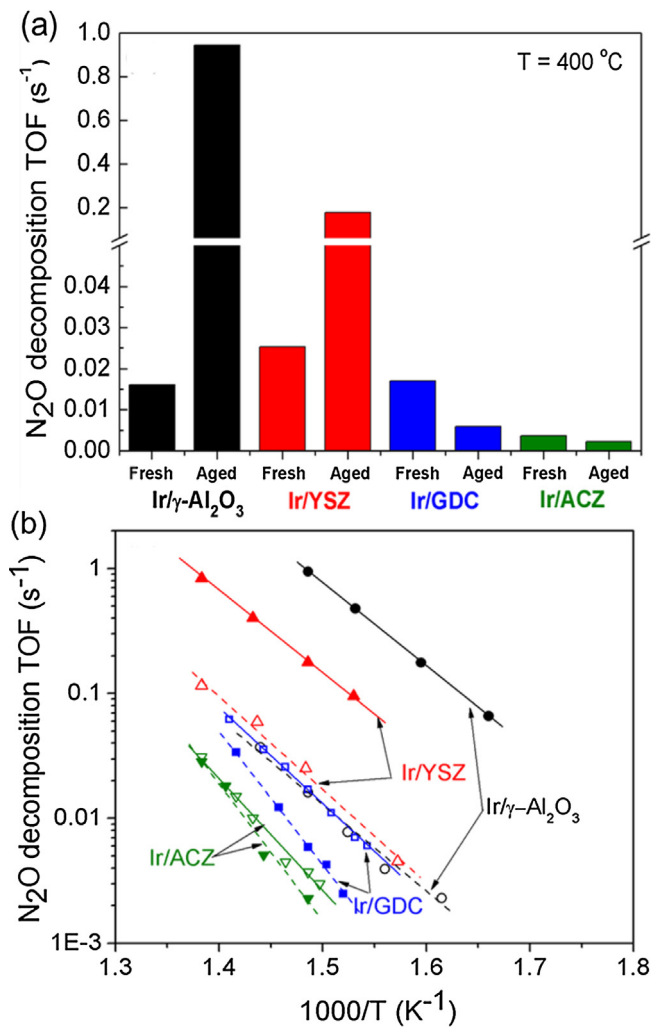


**Fig. 7.** (a) TOFs of fresh and aged catalysts at  $400^\circ\text{C}$ . (b) Arrhenius plots. Fresh = open symbols; aged = solid symbols.

of the well-established mechanism for  $\text{N}_2\text{O}$  dissociation over noble metal surfaces, which involves dissociative chemisorption of  $\text{N}_2\text{O}$  (Reaction (1)) followed by molecular  $\text{N}_2(\text{g})$  release and formation of adsorbed oxygen ( $\text{O}_{\text{ads}}$ ). The removal of the latter from the metal

**Table 3**

Activation energies of the rate constant for the  $\text{N}_2\text{O}$  decomposition reaction on the catalysts studied (conditions: 1000 ppm  $\text{N}_2\text{O}$  in  $\text{He}$ ; conversions less than 15%).

Catalyst	Activation energies (kJ/mol)	
	Fresh	Aged
$\text{Ir}/\gamma\text{-Al}_2\text{O}_3$	135.5	127.3
$\text{Ir}/\text{YSZ}$	144.6	123.7
$\text{Ir}/\text{GDC}$	148.5	206.1
$\text{Ir}/\text{ACZ}$	172.9	212.6

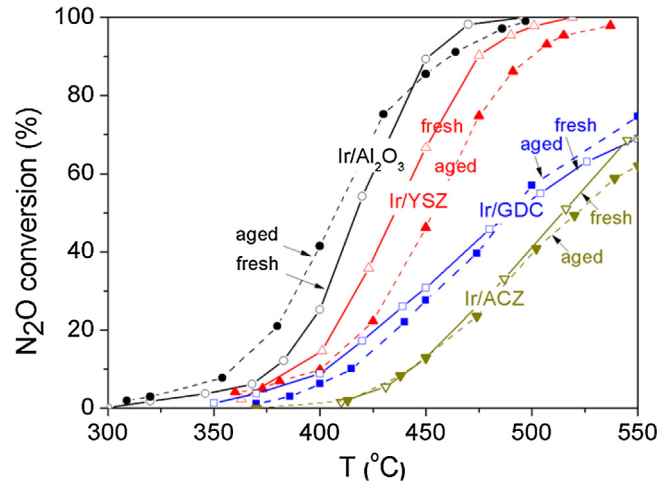


**Fig. 8.**  $\text{N}_2\text{O}$  conversion performance of the catalysts as a function of temperature (light-off diagram). Conditions:  $w_{\text{cat}} = 50 \text{ mg}$ ; Feed composition: 1000 ppm  $\text{N}_2\text{O}/\text{He}$ ,  $F_t = 150 \text{ cm}^3 \text{ min}^{-1}$ ; Weight hourly space velocity,  $\text{WHSV} = 180,000 \text{ cm}^3 \text{ g}^{-1} \text{ h}^{-1}$ .

surface then proceeds by recombination of  $\text{O}_{\text{ads}}$  to form  $\text{O}_2$  (Reaction (2)).



Thus weakening of both the  $\text{N}_2\text{O}_{\text{ads}}$  and  $\text{O}_{\text{ads}}$  chemisorption bonds due to oxygen spillover should inhibit Reaction (1) whilst also promoting Reaction (2). Our results indicate that in the present case the first effect predominates.

Reactant contact time ( $\tau$ ) defined as surface *Ir atoms per reactant molecule fed per second* affects the light-off behavior of catalysts [49] and is particularly important in the present case. This is because the aged catalysts have significantly different dispersions compared to their fresh counterparts, and correspondingly a very different number of active sites per gram of catalyst. Similar  $\tau$  values indicate similar probabilities for a reactant molecule to reach an active site. Taking the fresh and aged  $\text{Ir}/\gamma\text{-Al}_2\text{O}_3$  catalysts as an example, the  $\tau$  values corresponding to Fig. 8 are 15.7 s and 0.44 s respectively. The ratio  $\tau_{\text{fresh}}/\tau_{\text{aged}} = 15.7/0.44 \sim 36$ , implies that the loading of the aged catalyst would have to be 36 times higher than that of the fresh, in order to yield the same probability for an  $\text{N}_2\text{O}$  molecule to reach an active site in the two cases, assuming that no other factors are involved. In fact, the observed light-off performance of the aged  $\text{Ir}/\gamma\text{-Al}_2\text{O}_3$  sample (Fig. 8) was similar to that of the fresh sample, despite  $\tau$  being 36 times less in the former case, implying a much higher intrinsic activity (TOF) for the active sites present in the aged catalyst. This is in agreement with the results illustrated in Fig. 7 which show that the TOF was indeed far higher on large compared to small Ir particles. Importantly, the redox properties of the various supports suggest that the oxygen lability of ACZ is activated at significantly lower temperature ( $\sim 300^\circ\text{C}$ ) than that of GDC ( $\sim 500^\circ\text{C}$ ) (Fig. 1). This accounts for the greater inhibition of the de- $\text{N}_2\text{O}$  turnover rate caused by ACZ, as compared to that due

to GDC. In the temperature interval 350–550 °C, within which the N<sub>2</sub>O decomposition reaction was investigated, the oxygen lability of ACZ always exceeded that of GDC.

#### 4. Conclusions

Iridium-containing nanoparticles deposited on a variety of surfaces show thermal sintering characteristics that are very strongly correlated with the lability of lattice oxygen in the supporting oxide materials.

The higher the lability of oxygen ions in the support, the lower the vulnerability of the nanoparticles to sintering in an oxidative environment.

This resistance, or lack of resistance, to sintering may be rationalized in terms of oxygen spillover from support to nanoparticles.

Activity towards N<sub>2</sub>O decomposition is consistent with independently measured sintering characteristics. Observed turnover frequencies indicate that catalyst-support interactions were important in the cases of the sinter-resistant systems, an effect that may itself be linked to the phenomena that give rise to strong resistance to sintering.

Supports with high oxygen ion lability endow iridium catalyst nanoparticles with great resistance sintering in comparison to those that do not exhibit high oxygen ion lability.

#### Acknowledgements

MJT acknowledges Aston University for a PhD scholarship. GK acknowledges funding from the Royal Society and EPSRC. The authors would like to thank Dr C.M.A. Parlett and Dr M.A. Isaacs for their kind assistance with the TEM measurements.

#### References

- [1] S. Skaurai, H. Nishino, D.N. Futaba, S. Yasuda, T. Yamada, A. Maigne, Y. Matsuo, E. Nakamura, M. Yumura, H. Hata, *J. Am. Chem. Soc.* 134 (2012) 2148–2153.
- [2] A.D. Benavidez, L. Kovarik, A. Genc, N. Agrawal, E.M. Larsson, T.W. Hansen, A.M. Karim, A.K. Datye, *ACS Catal.* 2 (2012) 2349–2356.
- [3] S.B. Simonsen, I. Chorkendorff, S. Dahl, M. Skoglundh, J. Sehested, S. Helveg, *J. Catal.* 281 (2011) 147–155.
- [4] Z. Huang, X. Gu, Q. Cao, P. Hu, J. Hao, J. Li, X. Tang, *Angew. Chem. Int. Ed.* 51 (2012) 4198–4203.
- [5] R.M. Lambert, F.J. Williams, R.L. Cropley, A. Palermo, *J. Mol. Catal. A: Chem.* 228 (2005) 27–33.
- [6] R.B. Grant, R.M. Lambert, *J. Catal.* 92 (1985) 364–375.
- [7] Y. Nagai, K. Dohmae, Y. Ikeda, N. Takagi, T. Tanabe, N. Hara, G. Guilera, S. Pascarelli, M.A. Newton, O. Kuno, H. Jiang, H. Shinjoh, S. Matsumoto, *Angew. Chem. Int. Ed.* 47 (2008) 9303–9306.
- [8] M.A. Newton, C. Belver-Coldeira, A. Martínez-Arias, M. Fernández-García, *Nat. Mater.* 6 (2007) 528–532.
- [9] P. Granger, V.I. Parvulescu, *Chem. Rev.* 111 (2011) 3155–3207.
- [10] T.W. Hansen, A.T. Delariva, S.R. Challa, A.K. Datye, *Acc. Chem. Res.* 46 (2013) 1720–1730.
- [11] S.B. Simonsen, I. Chorkendorff, S. Dahl, M. Skoglundh, J. Sehested, S. Helveg, *J. Am. Chem. Soc.* 132 (2010) 7968–7975.
- [12] A.T. Delariva, T.W. Hansen, S.R. Challa, A.K. Datye, *J. Catal.* 308 (2013) 291–305.
- [13] W.-Z. Li, L. Kovarik, D. Mei, M.H. Engelhard, F. Gao, J. Liu, Y. Wang, C.H.F. Peden, *Chem. Mater.* 26 (2014) 5475–5481.
- [14] Q. Lin, Y. Huang, Y. Wang, L. Li, X.Y. Liu, F. Lv, A. Wang, W.-C. Lia, T. Zhang, *J. Mater. Chem. A* 2 (2014) 5178–5181.
- [15] J.C. Summers, S.A. Ausen, *J. Catal.* 58 (1979) 131–143.
- [16] M. Hatanaka, N. Takahashi, N. Takahashi, T. Tanabe, Y. Nagai, A. Suda, H. Shinjoh, *J. Catal.* 266 (2009) 182–190.
- [17] H. Hirata, K. Kishita, Y. Nagai, K. Dohmae, H. Shinjoh, S. Matsumoto, *Catal. Today* 164 (2011) 467–473.
- [18] S.J. Skinner, J.A. Kilner, *Mater. Today* 6 (2003) 30–37.
- [19] P. Vernoux, L. Lizarraga, M.N. Tsampas, F.M. Sapountzi, A. De Lucas-Consuegra, J.L. Valverde, S. Souentie, C.G. Vayenas, D. Tsipakides, S. Balomenou, E.A. Baranova, *Chem. Rev.* 113 (2013) 8192–8260.
- [20] J.-H. Lee, S.M. Yoon, B.-K. Kim, H.-W. Lee, H.S. Song, *J. Mater. Sci.* 37 (2002) 1165–1171.
- [21] H. He, H.X. Dai, C.T. Au, *Catal. Today* 90 (2004) 245–254.
- [22] D. Duprez, C. Descorme, T. Birchem, E. Rohart, *Top. Catal.* 16/17 (2001) 49–56.
- [23] G. Chiodelli, G. Flor, M. Scagliotti, *Solid State Ionics* 91 (1996) 109–121.
- [24] Y. Madier, C. Descorme, A.M. Le Govic, D. Duprez, *J. Phys. Chem. B* 103 (1999) 10999–11006.
- [25] A. Papavasiliou, A. Tsetsekou, V. Matsuka, M. Konsolakis, I.V. Yentekakis, *Appl. Catal. A Gen.* 382 (2010) 73–84.
- [26] D.J. Wuebbles, *Science* 326 (2009) 56–57.
- [27] A.R. Ravishankara, J.S. Daniel, R.W. Portmann, *Science* 326 (2009) 123–125.
- [28] S.A. Montzka, E.J. Dlugokencky, J.H. Butler, *Nature* 476 (2011) 43–50.
- [29] L. Li, J. Xu, J. Hu, J. Han, *Environ. Sci. Technol.* 48 (2014) 5290–5297.
- [30] C. Kroese, *Sci. Total Environ.* 143 (1994) 193–209.
- [31] F.J. Kapteijn, J. Rodriguez-Mirasol, J.A. Moulijn, *Appl. Catal. B Environ.* 9 (1996) 25–64.
- [32] G. Centi, A. Galli, B. Montanari, S. Perathoner, A. Vaccari, *Catal. Today* 35 (1997) 113–120.
- [33] G. Centi, S. Perathoner, F. Vazzana, M. Marella, M. Tomaselli, M. Mantegazza, *Adv. Environ. Res.* 4 (2000) 325–338.
- [34] W.B. Tolman, *Angew. Chem. Int. Ed.* 49 (2010) 1018–1024.
- [35] M. Konsolakis, *ACS Catal.* 5 (2015) 6397–6421.
- [36] C. Ohnishi, S. Iwamoto, M. Inoue, *Chem. Eng. Sci.* 63 (2008) 5076–5082.
- [37] S. Liu, Y. Cong, Y. Huang, X. Zhao, T. Zhang, *Catal. Today* 175 (2011) 264–270.
- [38] K. Yuzaki, T. Yarimizu, S. Ito, K. Kunimori, *Catal. Lett.* 47 (1997) 173–175.
- [39] A. Bueno-López, I. Such-Basáñez, C.J. Salinas-Martínez de Lecea, *J. Catal.* 244 (2006) 102–112.
- [40] H. Beyer, J. Emmerich, K. Chatziapostolou, K. Kohler, *Appl. Catal. A Gen.* 391 (2011) 411–416.
- [41] M. Konsolakis, C. Drosou, I.V. Yentekakis, *Appl. Catal. B Environ.* 123–124 (2012) 405–413.
- [42] E. Pachatouridou, E. Papista, E.F. Iliopoulos, A. Delimitis, G. Goula, I.V. Yentekakis, G.E. Marnellos, M. Konsolakis, *J. Environ. Chem. Eng.* 3 (2015) 815–821.
- [43] P.C. Flynn, S.E. Wanke, *J. Catal.* 34 (1974) 400–410.
- [44] C.G. Vayenas, S. Brosda, C.J. Pliangos, *J. Catal.* 216 (2003) 487–504.
- [45] J. Nicole, D. Tsipakides, C. Pliangos, X.E. Verykios, C. Comninellis, C.G. Vayenas, *J. Catal.* 204 (2001) 23–34.
- [46] J. Nicole, C. Comninellis, *J. Appl. Electrochem.* 28 (1998) 223–226.
- [47] S. Peng-Ont, S. Souentie, S. Assabumrungrat, P. Praserttham, S. Brosda, C.G. Vayenas, *Ionics* 19 (2013) 1705–1714.
- [48] Y. Nagai, T. Hirabayashi, K. Dohmae, N. Takagi, T. Minami, H. Shinjoh, S. Matsumoto, *J. Catal.* 242 (2006) 103–109.
- [49] I.V. Yentekakis, R.M. Lambert, M. Konsolakis, N. Kallithrakas-Kontos, *Catal. Lett.* 81 (2002) 181–185.